



1
2 **Surface elevation and ice thickness data between 2012 and 2020 at**
3 **the ablation area of Artesonraju Glacier, Cordillera Blanca, Perú.**

4 Jonathan Oberreuter¹, Edwin Badillo-Rivera^{2,3}, Edwin Loarte², Katy Medina², Alejo Cochachin⁴, José
5 Uribe¹

6 ¹Centro de Estudios Científicos (CECs), Valdivia, Chile.

7 ²Instituto Nacional de Investigación en Glaciares y Ecosistemas de Montaña (INAIGEM), Huaraz, Perú.

8 ³Facultad de Ingeniería Ambiental y Recursos Naturales, Universidad Nacional de Callao, Bellavista-Callao, Perú.

9 ⁴Área de Evaluación de Glaciares y Lagunas, Autoridad Nacional de Agua (ANA), Huaraz, Perú.

10

11 *Correspondence to:* Jonathan Oberreuter (jober@cecs.cl)

12 **Abstract.** We present a representative set of data of interpreted ice thickness and ice surface elevation at the ablation area of
13 the Artesonraju glacier between 2012 and 2020. The ice thickness was obtained by means of Ground Penetrating Radar
14 (GPR), while the surface elevation was by means of automated total stations and mass balance stakes. The data coverage is
15 about 14% of the whole glacier area. The results from GPR data show a maximum depth of 235 ± 18 m and a decreasing
16 mean depth ranging from 134 ± 18 m in 2013 to 110 ± 18 m in 2020. Additionally, we estimate a mean ice thickness change
17 rate of -4.2 ± 3.2 m yr⁻¹ between 2014 and 2020 with GPR data alone, which is in agreement with the elevation change in the
18 same period. The latter was estimated with the more accurate surface elevation data, yielding a change rate of -3.2 ± 0.2 myr⁻¹,
19 and hence, confirming a negative glacier mass balance. The data set can be valuable for further analysis when combined with
20 other data types, and as input for glacier dynamics modeling, ice volume estimations, and GLOF (glacial lake outburst flood)
21 risk assessment. The complete dataset is available at <https://doi.org/10.5281/zenodo.5571081> (Oberreuter et al, 2021).

22 **1 Introduction**

23 The glacier variations are sensitive to climate change (Oerlemans, 2005), particularly that of tropical glaciers (Rabatel et al.,
24 2013; Vuille et al., 2008) located between 23.43°N and 23.43°S, whose ablation processes occurs during the entire year,
25 while accumulation only during the austral summer (Gonzales Molina & Vacher, 2014). Hence, any variation in climate
26 affects tropical glaciers faster than glaciers from different latitudes (Uani, 2018). The tropical region of the Andes is
27 experiencing glacier mass loss since the end of Little Ice Age and has been accelerating since 1980 (Rabatel et al., 2013;
28 Unai, 2018), probably due to increase in air and ground temperatures. Vuille et al. (2015) showed an increase rate in air
29 temperature of 0.13°C per decade in the last 60 years, while Aguilar-Lome et al. (2019) showed that the ground temperature



30 increased at a rate of 0.17°C per decade above 5000 m.a.s.l., causing tropical glaciers to be the type with the most area
31 shrinkage globally at a rate of 1.6% per year (Li et al., 2019).

32 The tropical Andes concentrate ~99% of the tropical glaciers of the planet (Kaser & Osmaston, 2002), and of these, ~68%
33 are located in Perú (Veetil & Kamp, 2019), distributed in the 18 glacier cordilleras. The Artesonraju glacier is located in the
34 larger tropical glacier chain in the world: Cordillera Blanca, which concentrates ~40% of the Peruvian glacier surface, that is,
35 448.81 km² (INAIGEM, 2017), has a total length of 247 km (INAIGEM, 2018b) and it's simultaneously the cordillera with
36 the greater area glacier loss: 277.5 km² in the last 54 years (INAIGEM, 2018b). Also, it contributes ~40% of water supply to
37 the basin during dry season (Mark et al., 2005).

38 The glacier surface and volume reduction is in some cases associated with the generation of proglacial lakes and vice versa.
39 This association is stronger than that with land-terminating glaciers (King et al., 2018). Artesonraju glacier is one of those
40 cases, with an area reduction of 10% in 46 years, from 5.97 km² in 1970 (Ames, 1988) to 5.43 km² in 2016 (INAIGEM,
41 2018a). Its front has retreated 133 m in the period 2006-2019 (~10.2 m yr⁻¹), causing a severe expansion of the Artesoncocha
42 Alta lake, from 2,020 m² in 2003 to 22,314 m² in 2015 (INAIGEM, 2016).

43 In order to estimate the glacier ice thickness and its variations, several methods can be applied: ice-core drilling (Garzonio et
44 al., 2018; Zagorodnov et al., 2005), ice thickness modelling by means of: a) glacier morphology and slope (Campos, 2020;
45 Frey et al., 2014; Helfricht et al., 2019; Huss & Farinotti, 2012; Paul & Linsbauer, 2012), b) glacier surface velocities
46 (Gantayat et al., 2014; Sattar et al., 2019); and ice thickness measurement by means of geophysical methods such as seismics
47 and GPR (Booth et al., 2013; Colombero et al., 2019; Shean & Marchant, 2010; Zhao et al., 2016). GPR is a non-invasive
48 technique based on transmission and reception of radiowaves ranging normally from 10 MHz to 6 GHz (Zhao et al., 2016;
49 De Pascale et al., 2008), which has been successfully utilized in mountain glaciers for estimating ice thickness (Gacitúa et
50 al., 2015; Grab et al., 2021; Singh et al., 2010; Liu et al., 2020; Bohleber et al., 2017; Santin et al., 2019). However, up to
51 date, the GPR technique has been scarcely applied in tropical glaciers in Perú and the records of systematic monitoring in
52 Peruvian glaciers are also sparse. Hence, this study aims to contribute with ice thickness data and ice surface elevation data
53 at Artesonraju Glacier in Cordillera Blanca (Caraz-Áncash), from 2012 to 2020, which is useful for ice volume estimates and
54 as input for glacial dynamic models.

55 1.1 Study area

56 The study area comprises the Artesonraju glacier (Figure 1), a tropical glacier located in the northern side of the Cordillera
57 Blanca. According to the most recent national glacier inventory, its centroid is located at 8°57'29" S, 77°38'0" W, its
58 elevation ranges from 4902 to 5675 m.a.s.l. and an area of 5.43 km² (INAIGEM, 2016, 2018a). The ablation area of the
59 glacier consists of two parts: an uncovered part and a debris-covered part.

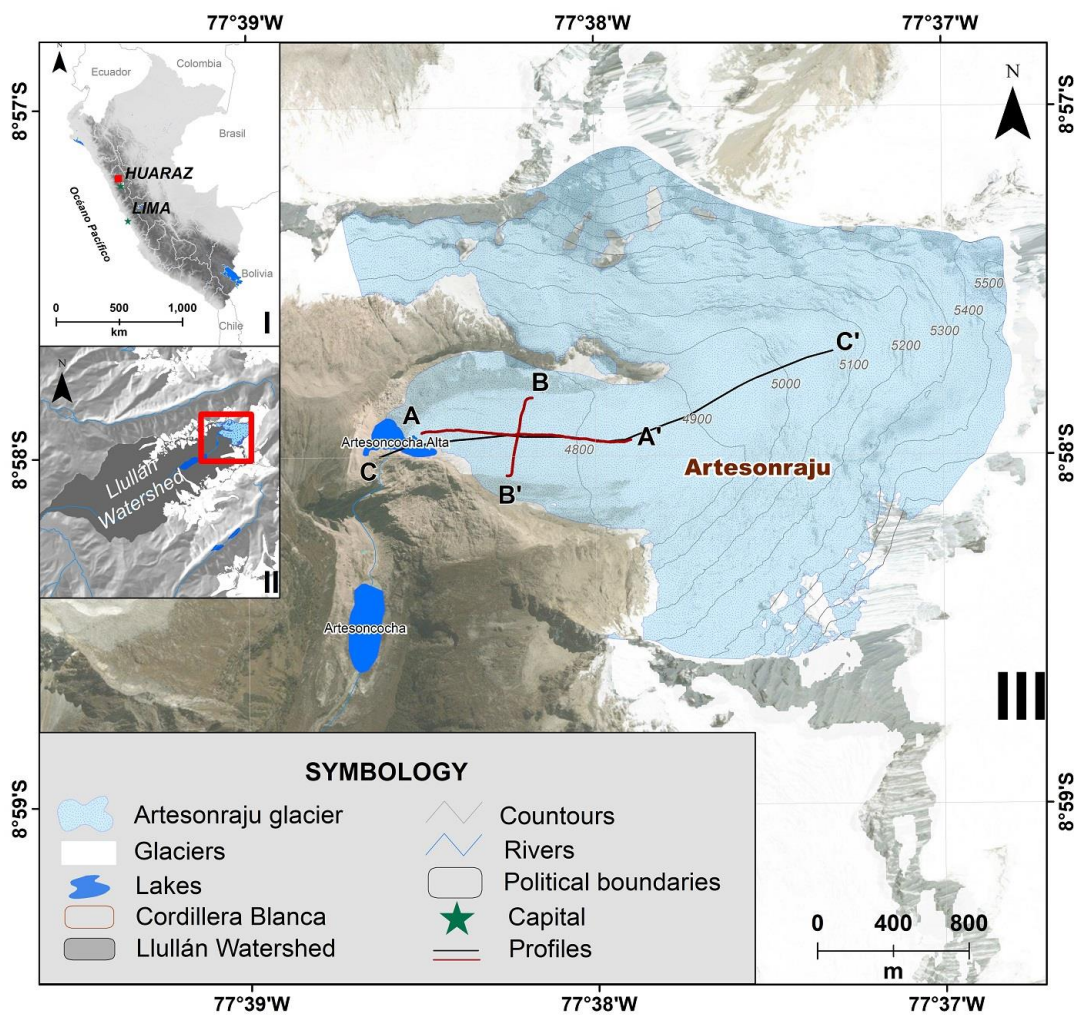


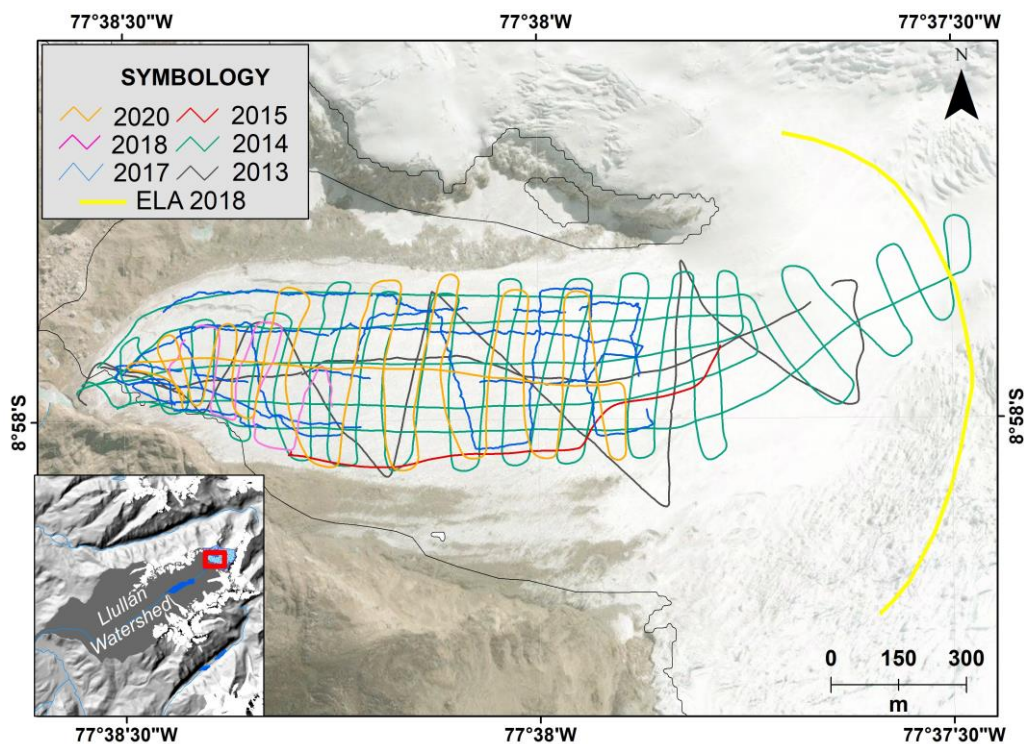
Figure 1 Study area of Artesonraju glacier. Glacier boundary from INAIGEM (2018a).

60
61

62 2 Data and methods

63 2.1 GPR data coverage

64 The GPR data coverage from 2013 to 2020 is described in Figure 2 and in Table 1. Data from years 2013-2017 were
65 collected by the Autoridad Nacional de Agua (ANA), while data from years 2018-2020 were collected by Instituto Nacional
66 de Investigación en Glaciares y Ecosistemas de Montaña (INAIGEM). All data were obtained with the same radar system
67 described in section 2.2.



68
 69 **Figure 2** GPR measurements coverage at Artesonraju glacier. Glacier boundary from INAIGEM (2018a). Background image:
 70 Landsat, 4th of July, 2014.

71 **Table 1** Ice thickness datasets used in this study.

Date	Collected by	Total profile length (km)	Coverage area as % of total area (5.43 km ²)
2013-07-11	ANA	5.3	12
2014-05-31/2014-06-03	ANA	18.6	14
2015-07-21	ANA	1.1	1
2017-05-30	ANA	8.0	7
2018-08-16	INAIGEM	1.4	1
2020-10-22	INAIGEM	6.8	7

72
 73 **2.2 GPR System**

74 A low-frequency impulse-type GPR developed by Unmanned Industrial LTDA has been used in order to estimate the ice
 75 depth, similar to the one used by Bello et al (2020) to measure the ice thickness on King George island in Antarctica. The
 76 GPR consists of a receiver, an impulse generator as transmitter, both with inbuilt GPS (Taoglas antenna, model AA.161) and



77 two bistatic-shaped antennas. Its main features are detailed in Table 2. The transmission unit is able to generate a high-
 78 voltage impulse at a pulse repetition frequency (PRF) of 1 kHz, with an output of 1.4 kV. Its two integrated GPS/GLONASS
 79 antennae (with GPS navigator accuracy) allow the trigger synchronization between receiver and transmitter, which is
 80 important for setting the beginning of each trace. The two antennas are dipole Wu-King type (Wu & King, 1965), with 5
 81 MHz of central frequency and bandwidth. During the capture process, the raw data are transferred to a handheld rugged
 82 computer (PDA) for storing and real-time visualization of data. For a better deploying of the GPR, a group of five people
 83 was needed during the surveys as shown in Figure 3.

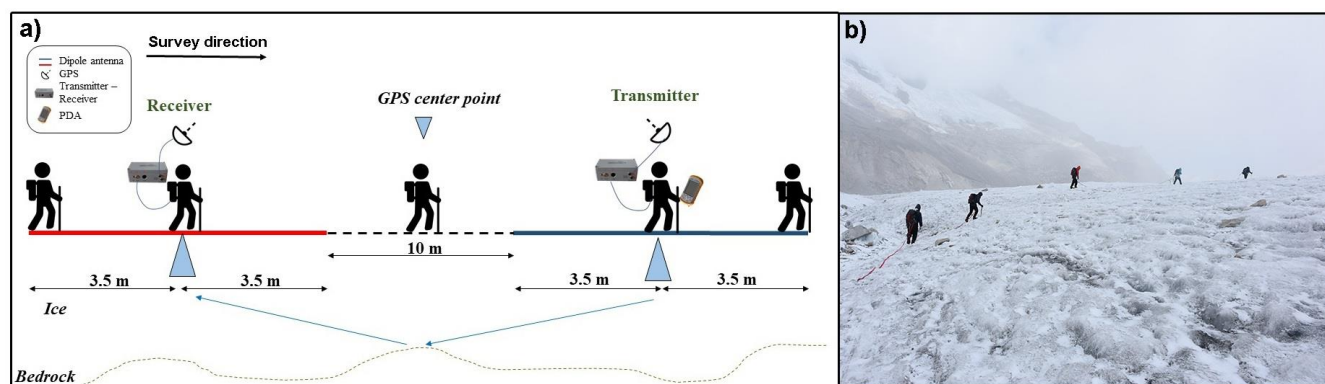
84 **Table 2 GPR features.**

Features	Value
Dipole length (m)	7
Transmitter voltage (kV)	1.4
Central frequency (MHz)	5
Sampling rate (MHz)	80
Range resolution (m)	16.8

85
 86 The receiver unit digitalizes the signal at a sampling rate of 80 MHz with 16 bits of resolution, yielding a sample length (or
 87 time increment) of 12.5 ns, and is able to stack from 256 to 4096 traces, with a trace length from 256 to 1024 samples. The
 88 digital system enables the user to set a fixed trace length (in samples) between 256 and 1024 (2^n format). The proper choice
 89 of the trace length depends on the estimated depth, ranging from 268 m to 1075 m, assuming a depth-averaged wave
 90 propagation velocity in ice (c) of 0.168 m/ns (Glen & Paren, 1975).

91 With the interpretation of the two-wave travel time ($TWTT$), we estimate the ice depth (h) using equation (1).

$$h = \frac{c * TWTT}{2} \quad (1)$$



92
 93 **Figure 3 a) GPR survey scheme performed in this study. The red and blue lines represent the dipole antennas of 7 m long each,**
 94 **with 10 m of spacing between the receiver and transmitter ends. b) GPR survey in the fieldwork at Artensonraju Glacier.**



95 **2.2 GPR data processing**

96 The first stage of the processing considers data preview and format conversion with the software RADAR View, which is the
97 software provided by the GPR company. Then, the files are able to be imported into software Reflexw, where profiles are
98 loaded and integrated with GPS data, and processing takes place, including the following steps:

99 a) Normalization of amplitude-saturated traces: Due to different sources of interference, traces are sometimes affected by
100 saturation in the signal amplitude, which leads visually to discontinuities in the profile. In this case, the normalization
101 consists of applying the calculation $\text{Amplitude}/\max(\text{Amplitude})$ to every trace.

102 b) Dewow filter: Low-pass filter used to eliminate the “wow” effect, caused by a low frequency component in the signal.
103 The filter is defined by a window length which should include the first arrival waveform. In this case, the window length
104 parameter was set to 100 ns, which satisfies the requirement.

105 c) Butterworth bandpass filter: To reduce the noise that is present in the signal outside the frequency range, where the radar
106 operates, which is centered at 5 MHz. The lower and higher boundaries of the filter were set to 2 and 10 MHz, respectively.

107 d) Definition of zero time: The direct wave travelling through the air between source and receiver should be eliminated in
108 order to estimate correctly the two wave travel times of the corresponding reflections. In this case, the zero time was equal
109 for each dataset varying from 305 ns to 380 ns.

110 e) Trace interpolation: To have a better visualization of the profile and as a necessary step for the migration, an equidistant
111 trace interpolation was performed. Here a 1 meter separation between traces was used, preserving a similar number of traces
112 per profile, and consequently, keeping the same horizontal resolution.

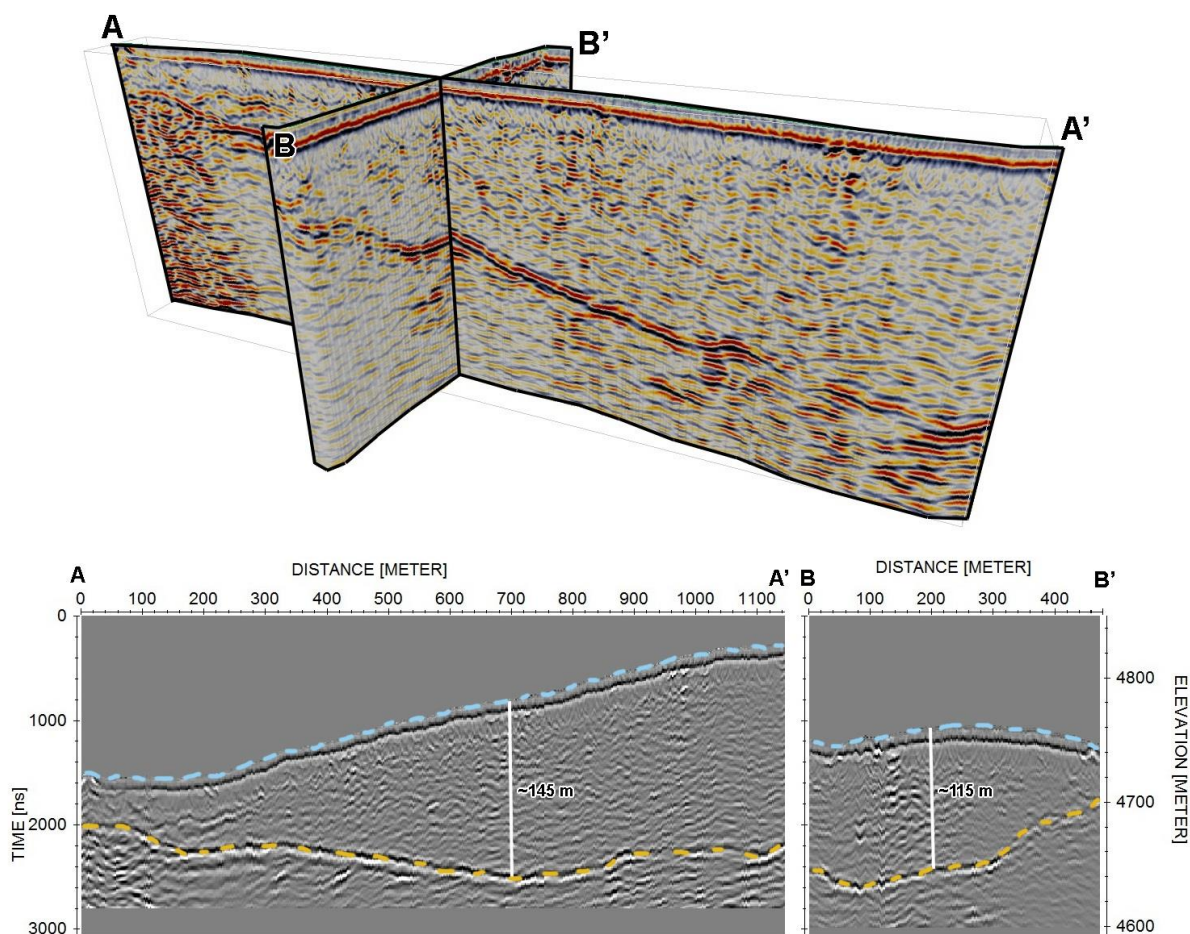
113 f) Migration: In order to set the reflectors to their real position, a migration process was performed. It was used a 1D
114 Kirchoff migration because of its better signal to noise ratio in this particular case. Here the migration profile window was
115 set to 250 traces and the depth-average electromagnetic wave velocity was set to 0.168 m/ns. This velocity was in agreement
116 with hyperbolae shapes.

117 g) Topographic correction: This procedure enables to move the traces up and down in the profile according to the elevation
118 that is store in the trace header, which was defined when importing the GPS data to the profile The results enable to visualize
119 correctly the surface elevation and the bedrock elevation along the profile (see lower panel of Figure 4).

120 After processing, the bedrock interface was manually picked at each radar profile and then exported to GIS software. The
121 processed radargrams are also visualized in OpendTect in order to examine the crossover differences. An example of two
122 processed profiles is shown in Figure 4. In general, there is good agreement in the crossover analysis (of the order of GPR
123 error), as shown in the upper inset of the figure.

124

125



126

127

128

129

130

Figure 4 Radargrams of Artesonraju glacier surveyed in 2020: profiles AA' and BB' as defined in Figure 1. Top panel shows a 3d view of longitudinal and transversal processed radar profiles (without topographic correction) and bottom panel shows the same processed profiles with topographic correction. The glacier surface is marked in color cyan and bedrock in yellow.

131

2.3 Surface and bedrock elevation

132

133

134

135

136

137

138

Two sets of surface elevation data, which were surveyed by ANA, are considered in this paper: first, 2012, 2014, 2018 and 2020 Digital Elevation Models (DEM) obtained from topographic points; and second, 2014, 2015, 2018 and 2019 mass balance stakes by means of automated total stations. The survey dates and coverage are detailed in Table 3. An automated total station is a total station that automatically and quickly follows the target (prism) with a laser while the radial topographic survey is being performed, facilitating the task in the fieldwork. The radial topographic survey is a source-to-receiver procedure, which aims to determine the position of several points over a surface, where the source is a total station with known reference position (XYZ coordinate) and elevation over the ground and the receiver is a prism with known



139 elevation over the surface. The total station estimates the source-receiver distance and angles in order to calculate the
140 position of the receiver in relation to the source position. In this study, one single source reference position was used for each
141 year, which was located outside the glacier area, at a fixed rock position of coordinates E=209143.7, N= 9007853.1, datum
142 WGS84, UTM18S, elevation: 4764.1 m.a.s.l. The elevation of the total station was estimated with navigator GPS and it was
143 used the same of each year. Then, each source-receiver surveyed with prism is stored within the memory of the total station.
144 Once the radial topographic survey has been completed, the data is downloaded and processed.
145 Topographic data from 2012 and 2014 were surveyed with a TOPCON model GPT 7005L (<https://www.al-top.com/producto/topcon-gpt-7005/>), while topographic data and mass balance stakes from 2015, 2017, 2018, 2019 and 2020
146 were acquired with help of a LEICA TS15 A 3" R400 (<https://surveyequipment.com/assets/index/download/id/844/>).
147 Considering the topographic survey data from 2012 to 2020, the number of points surveyed each year varies from 287 to 342
148 covering between 11% and 18% of the total glacier area (Table 3).When measuring the distances between nearest points of
149 every dataset, a mean value of ~25 m was found. In order to obtain the DEMs, the topographic points were converted to a
150 5m by 5 m raster and interpolated using the Inverse Distance Weighted interpolation tool in ArcGIS.
151 Due to better resolution and timespan of data, the first dataset was used to estimate the surface elevation changes of the
152 glacier, by subtracting the digital elevation model of 2020 from that of 2012.
153 In order to take advantage of the radar data coverage, the bedrock elevation was estimated by subtracting the ice thickness
154 interpretation from the surface elevation (base on the GPS of the radar survey) in every profile of the GPR data.
155

156 **Table 3 Surface elevation dataset used in this study.**

Date	Format	Number of points	Coverage area as % of total area (5.43 km ²)
2012-09-27	Points /Raster	321	12
2014-08-19	Points /Raster	287	13
2018-09-06	Points /Raster	386	18
2020-09-12	Points /Raster	342	11
2014-08-19	Mass balance stakes (Points)	14	3
2015-09-01	Mass balance stakes (Points)	16	3
2017-05-30	Mass balance stakes (Points)	19	4
2018-09-06	Mass balance stakes (Points)	18	5
2019-08-20	Mass balance stakes (Points)	15	4



157 **2.4 Errors**

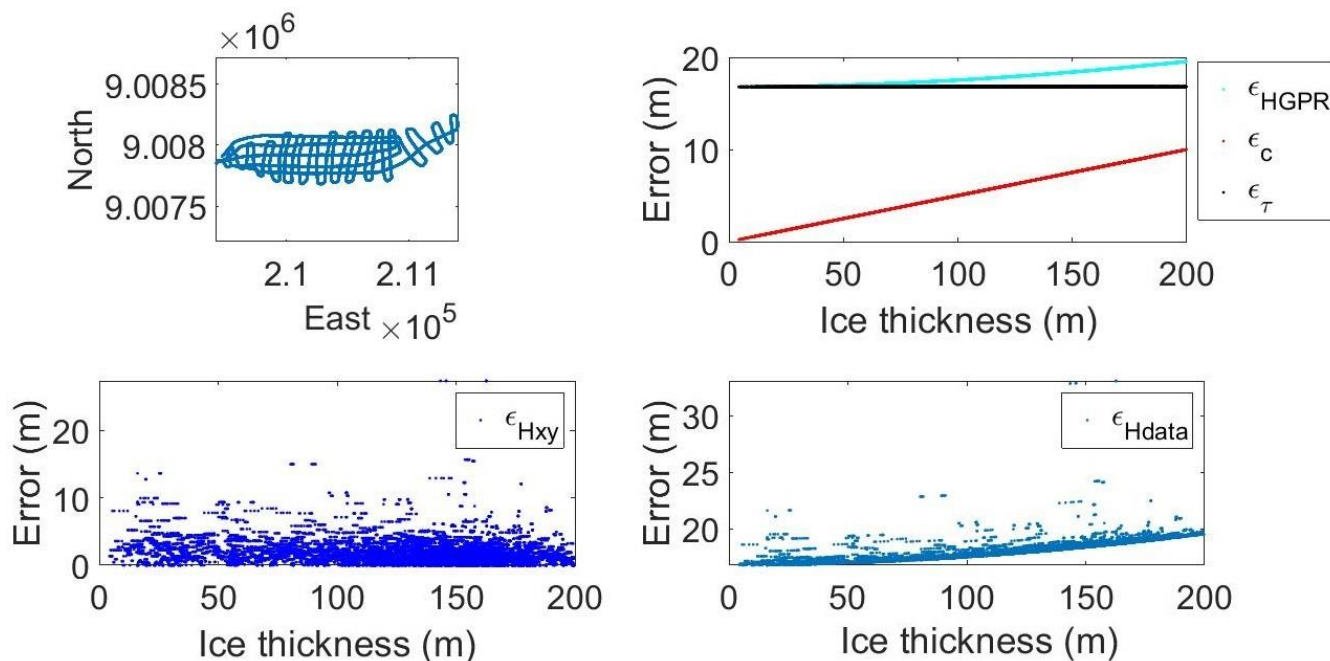
158 The estimation of errors in ice thickness (ϵ_{Hdata}) was obtained following Lapazaran et al. (2016), who split it into two
159 components: a) the error in the value of ice thickness due to GPR measurement (ϵ_{HGPR}), without taking into account where it
160 was obtained and b) the error in ice thickness due to uncertainties in horizontal positioning (ϵ_{Hxy}). ϵ_{Hdata} is variable and
161 hence, different for every GPR measurement point.

162 The term ϵ_{HGPR} is a function of the propagation velocity in ice (c) and its uncertainty (ϵ_c), TWTT, and timing error (ϵ_{τ}).
163 The velocity c is dependent of water content and ice purity. In this case, we set it to 0.168 m/ns as used by Gacitúa et al.
164 (2015) in mountain glacier Olivares Alfa in central Andes. Due to lack of measurements of c in tropical Andes, we assume a
165 high percentage of error of 5% in ϵ_c as suggested by Lapazaran et al (2016).

166 The term ϵ_{τ} is a function of the central frequency of the GPR (see Table 2) and c , which adds up 16.8 m.

167 The term ϵ_{Hxy} should be calculated considering the precision of GPS, speed of transportation and geometric aspects
168 (Lapazaran et al, 2016). ϵ_{Hxy} is then calculated a posteriori, unlike the other errors mentioned in this section, because an ice
169 thickness measurement is needed in order to estimate the error that applies on that measurement. In this case, we considered
170 5 meters of uncertainty in horizontal positioning because of the use of single frequency GPS (there was no dual frequency
171 GPS). With this uncertainty in the XY plane, a 5m by 5m cell point-to-raster for ice thickness procedure was performed,
172 estimating the difference between maximum and minimum interpreted ice thickness within each grid cell and then defining
173 this value as $\epsilon_{\text{Hxy}}/\sqrt{2}$.

174 An example of the estimated errors in ice thickness ϵ_{HGPR} , ϵ_{Hxy} and ϵ_{Hdata} for 2014 dataset is shown in Figure 5. Also, a
175 crossover analysis for the same dataset and for the whole ice thickness dataset is provided in Table 4. The analysis shows a
176 maximum difference of 10 meters, which is less than the radar resolution ϵ_{HGPR} .



177

178 **Figure 5** Estimated errors ϵ_{HGPR} , ϵ_{Hxy} and ϵ_{Hdata} for 2014 dataset, calculated according to Lapazaran et al (2016).

179

Table 4 Crossover analysis in ice thickness classified by year.

Crossover differences	2013	2014	2015	2017	2018	2020
Number of crossovers	8	109	0	22	0	15
Max (m)	9.4	9.3	No crossovers	6.5	No crossovers	13
Mean (m)	2.4	1.7	No crossovers	2.5	No crossovers	1.4
Std (m)	2.9	1.5	No crossovers	1.9	No crossovers	2.6
RMSD (m)	3.7	2.2	No crossovers	3.2	No crossovers	2.9

180

181 Regarding the surface elevation obtained by means of total stations, it has an error of ± 0.03 m, and then the surface
 182 difference estimations have a propagated error of ± 0.04 m.

183 In relation with radar data alone, the GPS elevation has an error of ± 15 m (Renfro et al, 2020) and the mean ice thickness
 184 error yields ± 18 m. Hence, the bedrock elevation has a propagated error of ± 23 m ($\sqrt{15^2 + 18^2}$). On the other hand, the ice
 185 thickness differences have a propagated error of ± 25.5 m.



186 In terms of glacier thinning rates, the propagated error is estimated by $\sqrt{\left(\frac{\delta t}{\Delta T}\right)^2 + \left(\frac{\delta y}{\Delta Y}\right)^2}$ where δt is the uncertainty in time,
187 ΔT is the time period, δy is the uncertainty in elevation/thickness difference, and ΔY is the elevation/thickness difference,
188 depending on which term may be used.

189 3 Results and discussion

190 This study presents the largest record of geophysical prospection using GPR at a glacier in the tropical Andes of Perú. The
191 overall length of radar profiles adds up 41.2 km covering a total surface of 0.85 km². The surface elevation of the profiles is
192 under the ELA, whose mean value between 2014 and 2019 yields 5016 m.a.s.l.

193 3.1 Surface elevation

194 The glacier surface elevations along profile CC' (Figure 1), which were obtained from interpolated DEMs and mass balance
195 stakes between 2012 and 2020, are presented in Figure 6(a). The elevation from available stakes measurements are in
196 agreement with that from DEMs (both data types are found in years 2014 and 2018).

197 Table 5 Surface elevation differences statistics.

DEM Difference	Period			
	2014-2012	2018-2014	2020-2018	2020-2012
Mean (m)	-5.8	-12.0	-7.9	-25.6
$\delta t/\Delta T$	25%	25%	25%	6%
Std (m)	1.3	1.9	3.0	3.6
$\delta y/\Delta Y$	22%	16%	38%	14%
Prop. Error	33%	30%	46%	15%
Mean/ ΔT (m yr ⁻¹)	-2.9±1.0	-3.0±0.9	-4.0±1.8	-3.2±0.5

198
199 In terms of elevation change for the periods 2012-2014, 2014-2018 and 2018-2020, mean differences of -5.8, -12.0 and -7.9
200 m were found, in the common area of the DEMs which mainly includes the ablation area. This leads to thinning rates of -
201 2.9±1.0 m yr⁻¹, -3.0±0.9 m yr⁻¹, and -4.0±1.8 m yr⁻¹, respectively (Table 5).

202 On the other hand, for the whole study period 2012-2020, a mean difference of -25.6 m with a standard deviation of 3.2 m
203 (13% of the absolute mean value) was found, as shown in Figure 6(b) and in Table 5. Assuming a temporal error of 0.5 years
204 (6% in the period 2012-2020), the propagated error adds up to 16%, yielding a surface elevation change of -3.2±0.5 m yr⁻¹ in
205 the ablation zone.

206

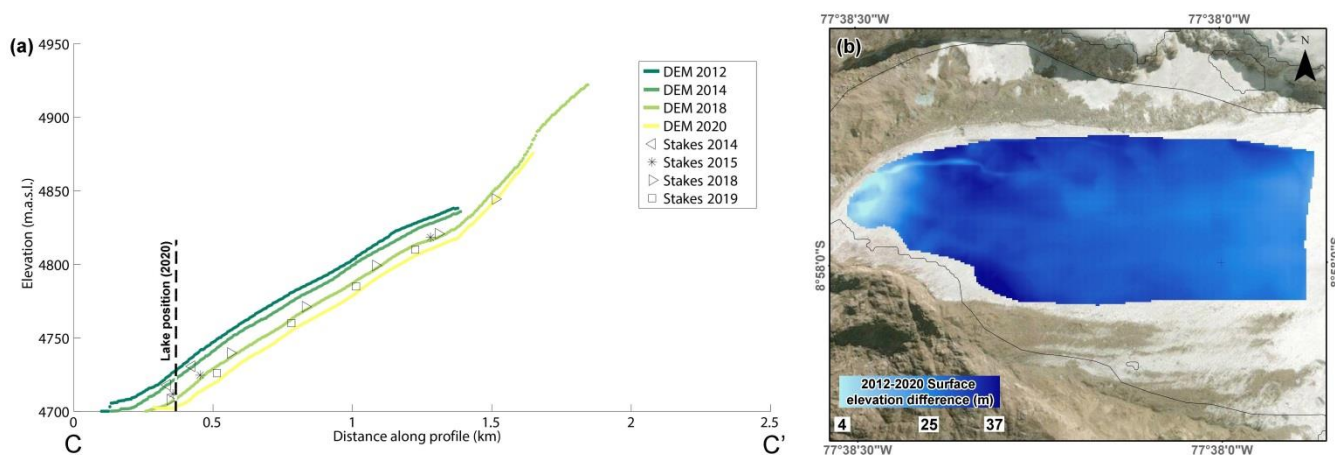


Figure 6 (a) Glacier surface elevation along profile CC' shown in Figure 1 and (b) surface elevation difference between 2012 and 2020, minimum: 4m, maximum: 37 m, mean difference: 25 m. Background image: Landsat, 4th of July, 2014.

3.2 Ice thickness data

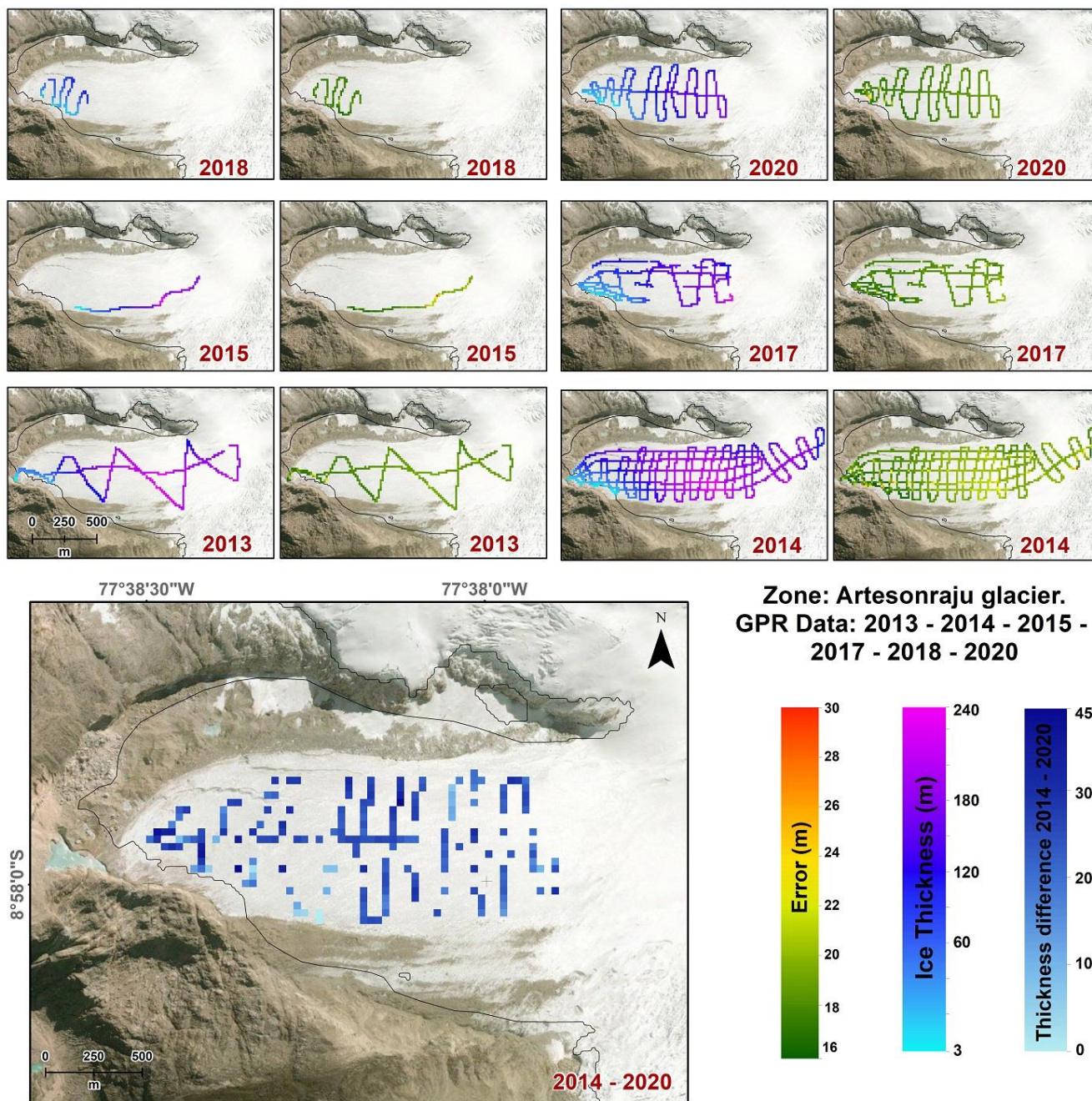
The interpreted ice thickness data at Artesonraju glacier from 2013 to 2020 as well as the 2014-2020 thickness difference are presented in Figure 7, while the main statistics of the interpreted data can be found in Table 6.

The main results show a maximum depth of $\sim 235 \pm 18$ m (2017), a minimum of $\sim 4 \pm 18$ m (2014, 2017) and a mean value that varies between 110 m (2020) and 134 m (2013). Data measured in 2018 have not been considered in the summary, due to their less spatial representability in this analysis.

The ice thickness differences between 2014 and 2020 shows a maximum difference of ~ 45 m and a mean value of ~ 25 m, with 18 m of mean error, yielding an ice thickness change rate of -4.2 ± 3.2 m yr⁻¹, which is in agreement with the surface elevation change estimations from section 3.1.

Table 6 Interpreted ice thickness data set statistics.

Ice thickness	Year					
	2013	2014	2015	2017	2018	2020
Mean (m)	134	133	129	118	69	110
Std (m)	1	1	1	1	1	1
Mean error (m)	19	19	19	18	18	18
Min (m)	6	4	41	4	17	5
Max (m)	195	200	202	235	112	183

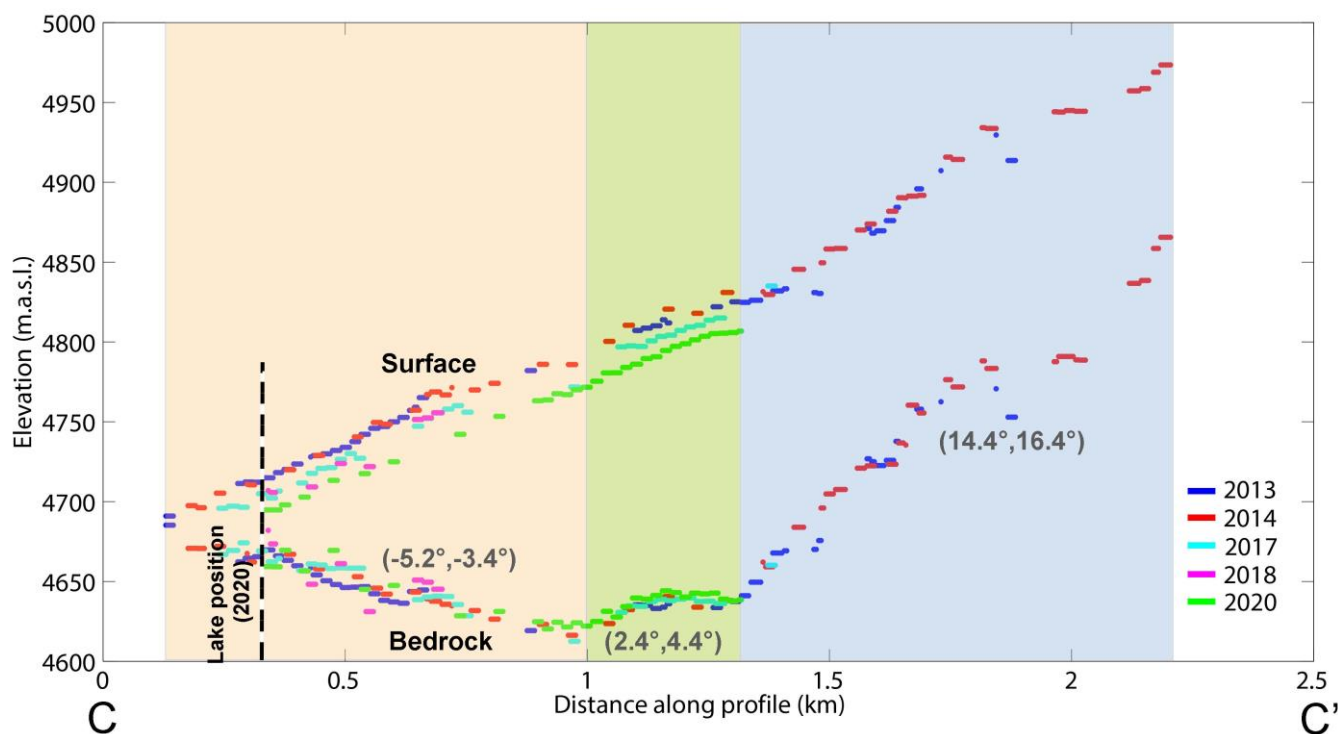


223
 224 **Figure 7 Interpreted ice thickness data (raster) from 2013 to 2020 and its error. Background image: Landsat, 4th of July, 2014.**

225
 226 The surface and bed elevation along profile CC' from 2013 to 2020 by means of radar measurements alone are shown in
 227 Figure 8. Also, an interpolated bedrock elevation is provided in Figure 9, using all subglacial elevation available. In the

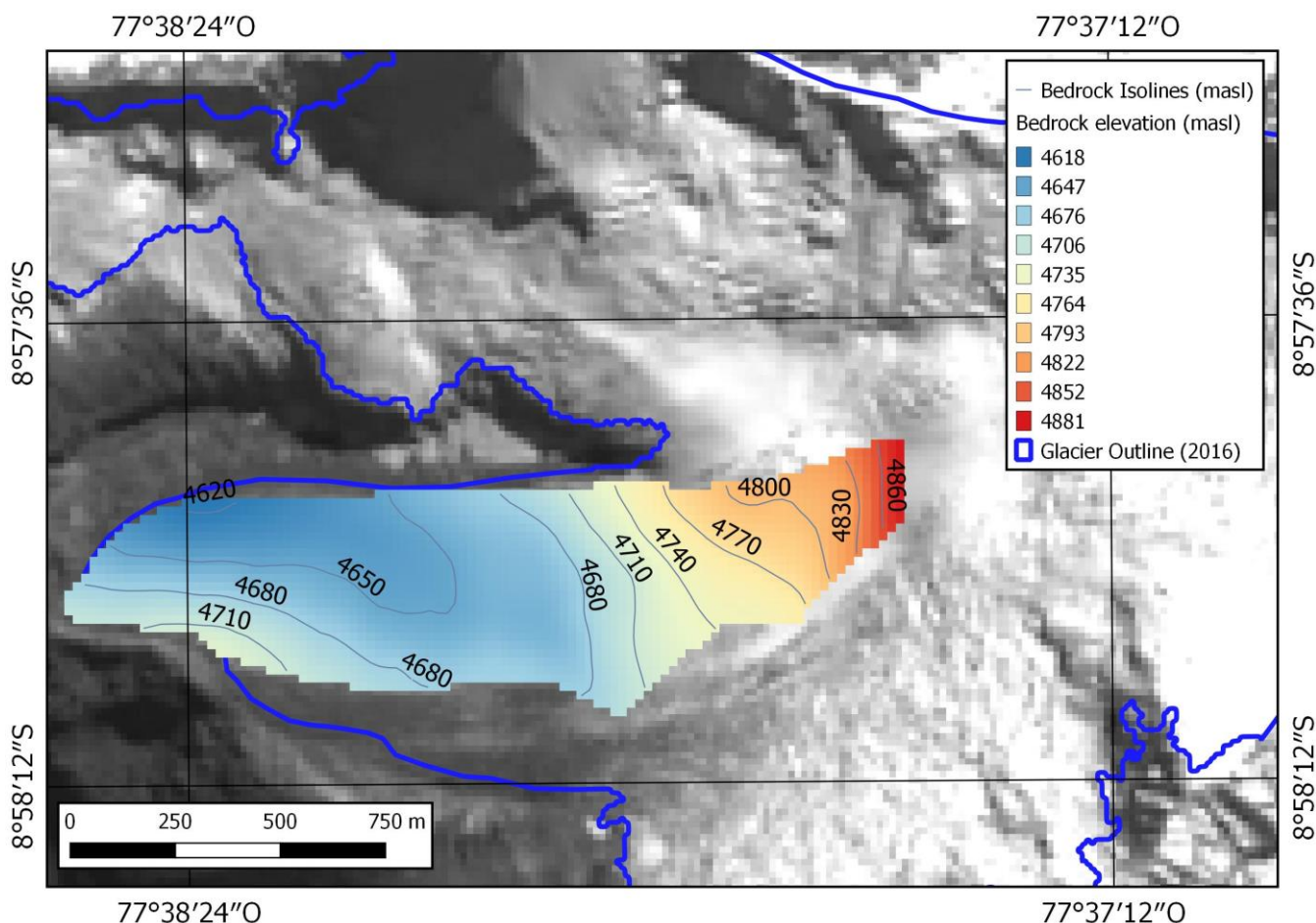


228 profile, the bedrock elevation ranges from 4613 m.a.s.l. to 4866 m.a.s.l. The results show a good agreement (within the
229 magnitude of error) in the bedrock elevation although the surveys are from different years. More evident changes could be
230 seen at the ablation zone of the glacier or glacier tongue, where the frontal recession is enabling the expansion of the lake
231 Artesoncocha Alta. Three zones along the CC' profile of Figure 8 can be identified: first, a clear overdeepening zone of the
232 glacier from the glacier front up to 1km upstream, with a bedrock slope between -5.2° and -3.4° , which can also be observed
233 in Figure 9; second, a smoothed positive zone, with bedrock slope between 2.4° and 4.4° ; and third, a more steep area with
234 bedrock slope between 14.4° and 16.4° . Similar morphological patterns at the bedrock were obtained by Chisolm (2016),
235 who estimated bed topography ranging from 4634 m.a.s.l. to 4893 m.a.s.l., indicating appropriate conditions for the
236 formation of a proglacial lake. The glacier frontal changes of $-10.2 \pm 2.0 \text{ m yr}^{-1}$ (INAIGEM, 2016) and the results obtained in
237 this study would indicate that in the following years the lake would advance up to the middle point of Artesonraju glacier
238 tongue, reaching a maximum depth of $82 \pm 18 \text{ m}$, estimated as the difference between the current lake surface elevation and
239 the elevation of the deepest part of the bedrock.



240
241
242

Figure 8 Surface and bedrock elevation along profile CC' from Figure 1.



243
244 **Figure 9** Bedrock model from all GPR measurements (2013 to 2020). The result was smoothed with a gaussian filter in order to
245 eliminate artifacts that may be generated. Background image: Landsat, 12 July, 2014.

246 5 Conclusions

247 We provide a robust dataset contributing with interpreted ice thickness data and ice surface elevation data at the ablation area
248 of Artesonraju glacier in Caraz-Áncash, from 2012 to 2020. Data analysis reveals two aspects: a) a strong decadal mass
249 balance reduction and b) the existence of an overdeepening up to 700 m upstream the central flowline, which may lead to an
250 expansion of lake Artesoncocha Alta up to that point. Data here provided is useful as input for glacier dynamics modelling
251 and can be complemented with other data types for further analysis. It is also necessary to assess the risks associated with the
252 volume increase of the proglacial lake Artesoncocha Alta and with GLOF generation, which may constitute a hazard for the
253 communities located downstream the Artesonraju glacier.



254 **Data availability**

255 The datasets used in this paper are available at <https://doi.org/10.5281/zenodo.5571081> (Oberreuter et al, 2021).

256 The ice thickness data consists of vector files (*.shape) with the following fields: tr: trace number within the processed
257 profile; x: East coordinates in WGS84/18S, y: North coordinates in WGS84/18S, z: glacier surface elevation (meters above
258 sea level), z: tau_r: two way travel time, depth: ice thickness using 0.168 m/ns, zb: glacier bed elevation (z-depth),
259 e_H_GPR: error in ice thickness due to GPR measurement (ϵ_{HGPR}), e_H_xyf: error in ice thickness due to horizontal
260 positioning (ϵ_{Hxy}), e_H_data: total error in ice thickness (ϵ_{Hdata}).

261 The surface elevation data from total stations consists of: a) vector files (*.shape) with the following fields: ID, East: East
262 coordinates in WGS84/18S, North: North coordinates in WGS84/18S, H_masl: surface elevation in meters (above sea level),
263 Class: point classification; b) raster files (.tif) with the interpolated surface elevation.

264 The stakes surface elevation consists of vector files (*.shape) with the following fields: Name: name of the stake, North:
265 North coordinates in WGS84/18S, East: East coordinates in WGS84/18S, H_masl: surface elevation in meters (above sea
266 level).

267 **Author contributions**

268 INAIGEM and ANA collected the data. JO processed, interpreted the radar data, conception of the work, data analysis and
269 elaboration of figures. EB contributed with the design of the work, data analysis and elaboration of figures, EL contributed
270 with the design of the work and critical revision of the article, KM contributed with the design of the work and critical
271 revision of the article, AC contributed with the design of the work and critical revision of the article, and JU contributed with
272 technical review.

273 **Competing interests**

274 The authors declare that they have no conflict of interest.

275 **Acknowledgments**

276 The authors acknowledge financial support from Concytec, the British Embassy, NERC and the Newton-Paulet Fund within
277 the framework of the call E031-2018-01-NERC "Glacier Research Circles", through its executing unit ProCiencia [Contract
278 N°08-2019-FONDECYT] of Peru GROWS project. Also, the authors acknowledge the financial support from the Concytec -
279 World Bank Project "Improvement and Expansion of the National Science Technology and Technological Innovation
280 System Services" 8682-PE, through its executing unit ProCiencia [Contract N°23-2018-FONDECYT-BM-IADT-MU] of
281 Permafrost project.



282

283 **References**

284

285 Aguilar-Lome, J., Espinoza-Villar, R., Espinoza, J. C., Rojas-Acuña, J., Willems, B. L., & Leyva-Molina, W. M. Elevation-
286 dependent warming of land surface temperatures in the Andes assessed using MODIS LST time series (2000–2017).
287 International Journal of Applied Earth Observation and Geoinformation, 77(April 2018), 119–128.
288 <https://doi.org/10.1016/j.jag.2018.12.013>, 2019.

289 Ames, A. Inventario de Glaciares del Perú. (Vol. 1), 1988.

290 ANA. Estudio: Evaluación de la disponibilidad de recursos hídricos en glaciares en un contexto de cambio climático en las
291 cordilleras Blanca, Central, Huaytapallana, Ampato y Vilcanota, 2019.

292 Bello, C., Santillán, N., Cochachín, A., Arias, S., & Suarez, W. Ice thickness using ground penetrating radar at Znosko
293 glacier on King George Island. International Archives of the Photogrammetry, Remote Sensing and Spatial Information
294 Sciences - ISPRS Archives, 42(3/W12), 437–439. 2020

295 Bohleber, P., Sold, L., Hardy, D. R., Schwikowski, M., Klenk, P., Fischer, A., Sirguey, P., Cullen, N. J., Potocki, M.,
296 Hoffmann, H., and Mayewski, P.: Ground-penetrating radar reveals ice thickness and undisturbed englacial layers at
297 Kilimanjaro's Northern Ice Field, The Cryosphere, 11, 469–482, <https://doi.org/10.5194/tc-11-469-2017>, 2017.

298 Booth, A. D., Mercer, A., Clark, R., Murray, T., Jansson, P., & Axtell, C. A comparison of seismic and radar methods to
299 establish the thickness and density of glacier snow cover. Annals of Glaciology, 54(64), 73–82.
300 <https://doi.org/10.3189/2013AoG64A044>, 2013.

301 Campos, N. Revisión de procedimientos metodológicos para la reconstrucción glaciaria y el cálculo de la altitud de la línea de
302 equilibrio. Revista de Geografía Norte Grande, 350(76), 321–350. <https://doi.org/10.4067/s0718-34022020000200321>,
303 2020.

304 Chisolm, R. E. Climate Change Impacts and Water Security in the Cordillera Blanca, Perú. 328pp, 2016.

305 Colombero, C., Comina, C., De Toma, E., Franco, D., & Godio, A. Ice thickness estimation from geophysical investigations
306 on the terminal lobes of Belvedere Glacier (NW Italian Alps). Remote Sensing, 11(7), 1–19.
307 <https://doi.org/10.3390/rs11070805>, 2019.

308 De Pascale, G., Pollard, W., & Williams, K. Geophysical mapping of ground ice using a combination of capacitive coupled
309 resistivity and ground-penetrating radar, Northwest Territories, Canada. Journal of Geophysical Research, 113 (F02S90),
310 <https://doi.org/10.1029/2006JF000585>, 2008.

311 Frey, H., Machguth, H., Huss, M., Huggel, C., Bajracharya, S., Bolch, T., Kulkarni, A., Linsbauer, A., Salzmann, N., &
312 Stoffel, M. Estimating the volume of glaciers in the Himalayan-Karakoram region using different methods. Cryosphere,
313 8(6), 2313–2333. <https://doi.org/10.5194/tc-8-2313-2014>, 2014.



- 314 Gacitúa, G., Uribe, J., Wilson, R., Loriaux, T., Hernández, J., & Rivera, A. 50 MHz helicopter-borne radar data for
315 determination of glacier thermal regime in the central Chilean Andes. *Annals of Glaciology*, 56(70), 2015.
- 316 Gantayat, P., Kulkarni, A. V., & Srinivasan, J. Estimation of ice thickness using surface velocities and slope: Case study at
317 Gangotri Glacier, India. *Journal of Glaciology*, 60(220), 277–282. <https://doi.org/10.3189/2014JoG13J078>, 2014.
- 318 Garzonio, R., Di Mauro, B., Strigaro, D., Rossini, M., Colombo, R., De Amicis, M., & Maggi, V. Mapping the suitability for
319 ice-core drilling of glaciers in the European Alps and the Asian High Mountains. *Journal of Glaciology*, 64(243), 12–26.
320 <https://doi.org/10.1017/jog.2017.75>, 2018.
- 321 Glen, J.W., and Paren, J.G. The electrical properties of snow and ice: *Journal Of Glaciology*, v. 15, no. 73, p. 15–38, 1975.
- 322 Gonzales Molina, S., & Vacher, J.-J. El Perú frente al cambio climático: Resultados de investigaciones franco-peruanas
323 (IRD). <https://doi.org/10.4000/books.irdeditions.19580>, 2014.
- 324 Grab, M., Mattea, E., Bauder, A., Huss, M., Rabenstein, L., Hodel, E., et al. Ice thickness distribution of all Swiss glaciers
325 based on extended ground-penetrating radar data and glaciological modeling. *Journal of Glaciology*. 1-
326 19, <https://doi.org/10.1017/jog.2021.55>, 2021.
- 327 Helfricht, K., Huss, M., Fischer, A., & Otto, J. C. Calibrated ice thickness estimate for all glaciers in Austria. *Frontiers in*
328 *Earth Science*, 7(April), 1–15. <https://doi.org/10.3389/feart.2019.00068>, 2019.
- 329 Huss, M., & Farinotti, D. Distributed ice thickness and volume of all glaciers around the globe. *Journal of Geophysical*
330 *Research: Earth Surface*, 117(4). <https://doi.org/10.1029/2012JF002523>, 2012.
- 331 INAIGEM. Reconocimiento peligros naturales en la laguna nueva Artesoncocha Alta, 2016.
- 332 INAIGEM. Manual metrológico para el inventario nacional de glaciares, 2017.
- 333 INAIGEM. Geoportal INAIGEM. <https://visor.inaigem.gob.pe/>, 2018a.
- 334 INAIGEM. Las Cordilleras Glaciares del Perú. In Ministerio del Ambiente (Vol. 1, Issue 9), 2018b.
- 335 Kaser, G., & Osmaston, H. *Tropical Glaciers*, 2002.
- 336 King, O., Dehecq, A., Quincey, D., & Carrivick, J. Contrasting geometric and dynamic evolution of lake and land-
337 terminating glaciers in the central Himalaya. *Global and Planetary Change*, 167, 46–60.
338 <https://doi.org/10.1016/j.gloplacha.2018.05.006>, 2018.
- 339 Lapazaran, J., Otero, J., Martín-Español, A. & Navarro, F.J. On the errors involved in ice-thickness estimates I: ground-
340 penetrating radar measurement errors. *J. Glaciol.*, 2016.
- 341 Li, Y., Ding, Y.-J., Shangguan, D.-H., & Wang, R.-J. Regional differences in global glacier retreat from 1980 to 2015.
342 *Advances in Climate Change Research*, 10(4), 203–213. <https://doi.org/10.1016/j.accre.2020.03.003>, 2019.
- 343 Liu, J., Wang, S., He, Y., Li, Y., Wang, Y., Wei, Y., Che, Y. Estimation of Ice Thickness and the Features of Subglacial
344 Media Detected by Ground Penetrating Radar at the Baishui River Glacier No. 1 in Mt. Yulong, China. *Remote*
345 *Sens.*, 12, 4105. <https://doi.org/10.3390/rs12244105>, 2020.



- 346 Mark, B. G., McKenzie, J. M., & Gómez, J. Hydrochemical evaluation of changing glacier meltwater contribution to stream
347 discharge: Callejon de Huaylas, Perú. *Hydrological Sciences Journal*, 50(6), 975–988.
348 <https://doi.org/10.1623/hysj.2005.50.6.975>, 2005.
- 349 Oberreuter, J., Badillo-Rivera, E., Loarte, E., Medina, K., Cochachín, A. & Uribe, J. (2021). Surface elevation (2012-2020)
350 and ice thickness (2014-2020) datasets measured at Artesonraju Glacier, Cordillera Blanca, Perú [Data set]. Zenodo.
351 <https://doi.org/10.5281/zenodo.5571082>
- 352 Oerlemans, J. Atmospheric science: Extracting a climate signal from 169 glacier records. *Science*, 308(5722), 675–677.
353 <https://doi.org/10.1126/science.1107046>, 2005.
- 354 Paul, F., & Linsbauer, A. Modeling of glacier bed topography from glacier outlines, central branch lines, and a DEM.
355 *International Journal of Geographical Information Science*, 26(7), 1173–1190.
356 <https://doi.org/10.1080/13658816.2011.627859>, 2012.
- 357 Rabatel, A., Francou, B., Soruco, A., Gomez, J., Cáceres, B., Ceballos, J. L., Basantes, R., Vuille, M., Sicart, J. E., Huguel,
358 C., Scheel, M., Lejeune, Y., Arnaud, Y., Collet, M., Condom, T., Consoli, G., Favier, V., Jomelli, V., Galarraga, R., ...
359 Wagnon, P. Current state of glaciers in the tropical Andes: A multi-century perspective on glacier evolution and climate
360 change. *Cryosphere*, 7(1), 81–102. <https://doi.org/10.5194/tc-7-81-2013>, 2013.
- 361 Renfro, B., Stein, M., Reed, E., Morales, J. and Villalba, E. An Analysis of Global Positioning System (GPS) Standard
362 Positioning System (SPS) Performance for 2019. Austin, TX, 2020.
- 363 Rutishauser, A., Maurer, H., & Bauder, A. Helicopter-borne ground-penetrating radar investigations on temperate alpine
364 glaciers: A comparison of different systems and their abilities for bedrock mapping. *Geophysics*, 81(1), P. WA119-
365 WA129, 2016.
- 366 Santin, I., Colucci, R. R., Žebre, M., Pavan, M., Cagnati, A., & Forte, E. Recent evolution of Marmolada glacier (Dolomites,
367 Italy) by means of ground and airborne GPR surveys. *Remote Sensing of Environment*, 235(August).
368 <https://doi.org/10.1016/j.rse.2019.111442>, 2019.
- 369 Sattar, A., Goswami, A., Kulkarni, A. V., & Das, P. Glacier-surface velocity derived ice volume and retreat assessment in
370 the dhauliganga basin, central himalaya – A remote sensing and modeling based approach. *Frontiers in Earth Science*,
371 7(May), 1–15. <https://doi.org/10.3389/feart.2019.00105>, 2019.
- 372 Shean, D. E., & Marchant, D. R. Seismic and GPR surveys of Mullins Glacier, mcmurdo dry valleys, Antarctica: Ice
373 thickness, internal structure and implications for surface ridge formation. *Journal of Glaciology*, 56(195), 48–64.
374 <https://doi.org/10.3189/002214310791190901>, 2010.
- 375 Singh, K., Kulkarni, A., & Mishra, V. Estimation of glacier depth and moraine cover study using ground penetrating radar
376 (GPR) in the Himalayan region. *J Indian Soc Remote Sens* 38, 1–9. <https://doi.org/10.1007/s12524-010-0001-2>, 2010.
- 377 Unai, A. Evolución del Balance de Masas y Retroceso Glaciar en el Nevado Artesonraju (Cordillera Blanca, Perú).
378 <https://addi.ehu.es/handle/10810/30075>, 2018.



- 379 Veettil, B. K., & Kamp, U. Global disappearance of tropical mountain glaciers: Observations, Causes, and Challenges.
380 Geosciences (Switzerland), 9(5), 1–25. <https://doi.org/10.3390/geosciences9050196>, 2019.
- 381 Vuille, M., Francou, B., Wagnon, P., Juen, I., Kaser, G., Mark, B. G., & Bradley, R. S. Earth-Science Reviews Climate
382 change and tropical Andean glaciers : Past, present and future. 89, 79–96. <https://doi.org/10.1016/j.earscirev.2008.04.002>,
383 2008.
- 384 Vuille, M., Franquist, E., Garreaud, R., Lavado Casimiro, W. S., & Cáceres, B. Impact of the global warming hiatus on
385 Andean temperature. Journal of Geophysical Research: Atmospheres, 120, 1–17.
386 <https://doi.org/10.1002/2014JC010485>. Received, 2015.
- 387 Wu, T., and King, R. The cylindrical antenna with nonreflecting resistive loading: IEEE Transactions on Antennas and
388 Propagation, v. 13, no. 3, p. 369–373, 1965
- 389 Zagorodnov, V., Thompson, L. G., Ginot, P., & Mikhalenko, V. Intermediate-depth ice coring of high-altitude and polar
390 glaciers with a lightweight drilling system. Journal of Glaciology, 51(174), 491–501.
391 <https://doi.org/10.3189/172756505781829269>, 2005.
- 392 Zhao, W., Forte, E., Colucci, R. R., & Pipan, M. High-resolution glacier imaging and characterization by means of GPR
393 attribute analysis. Geophysical Journal International, 206(2), 1366–1374. <https://doi.org/10.1093/gji/ggw208>, 2016.